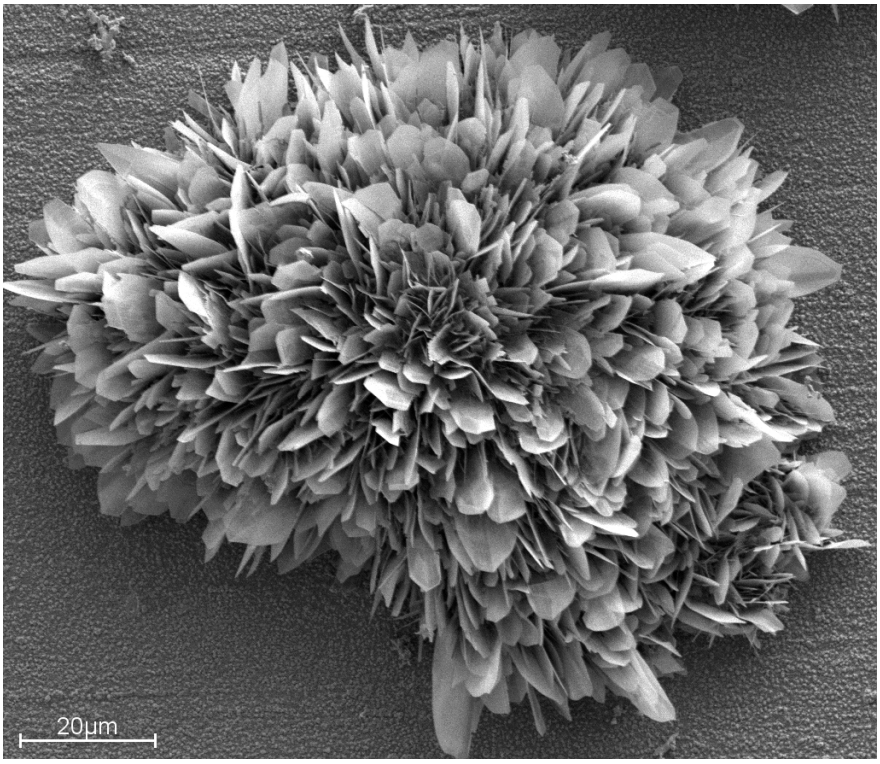
CHALMERS
UNIVERSITY OF TECHNOLOGY



Dual Atmosphere Corrosion of Ferritic Stainless Steel used for Solid Oxide Fuel Cell Applications

The Importance of the Location of Pre-Oxidation Scales

Master's thesis in Material's Chemistry

ROBIN FAUST

Department of Chemistry and Chemical Engineering
Chalmers University of Technology
Gothenburg, Sweden 2017

MASTER'S THESIS 2017

Dual Atmosphere Corrosion of Ferritic Stainless Steel used for Solid Oxide Fuel Cell Applications

The Importance of the Location of Pre-Oxidation Scales

ROBIN FAUST



CHALMERS
UNIVERSITY OF TECHNOLOGY

Department of Chemistry and Chemical Engineering
Competence Center for High Temperature Corrosion
CHALMERS UNIVERSITY OF TECHNOLOGY
Gothenburg, Sweden 2017

Dual Atmosphere Corrosion of Ferritic Stainless Steel used for Solid Oxide Fuel Cell Applications
The Importance of the Location of Pre-Oxidation Scales
ROBIN FAUST

© ROBIN FAUST, 2017.

Supervisor: Claudia Göbel, HTC
Examiner: Jan Froitzheim, HTC

Master's Thesis 2017
Department of Chemistry and Chemical Engineering
Competence Center for High Temperature Corrosion
Chalmers University of Technology
SE-412 96 Gothenburg
Telephone +46 31 772 1000

Abstract

Ferritic stainless steel used for SOFC interconnects was exposed to a simulated fuel cell atmosphere. The samples investigated were pre-oxidized for 11 minutes or 3 hours at 800 °C. Subsequently, the thereby grown protective oxide layers were removed from one side, prior to the exposure. The exposure was conducted at 600 °C in dual atmosphere (hydrogen on one side, air on the other side). The experiment was interrupted after certain time intervals to check for corrosion. The total exposure lasted up to 1000 hours.
Afterwards, the samples were investigated with electron microscopy in order to determine the severeness of the subsequent breakaway corrosion.

Contents

Abbreviations **iii**

1 Introduction **1**
1.1 Fuel Cells 1
1.2 Interconnect 4
1.3 Corrosion 4
1.3.1 Corrosion Protection 7
1.3.2 Chromium Evaporation 8
1.4 Influence of Surface Conditions 9
1.5 Dual Atmosphere and Inverse Temperature Effect 11
1.6 Aim 12

2 Experimental **13**
2.1 Samples 13
2.2 Experimental setup 14
2.3 Analytical Methods 16
2.3.1 Cross-section Preparation 16
2.4 Microscopy Analysis 16

3 Results and Discussion **18**
3.1 Run 1 18
3.1.1 Visual Inspection 18
3.1.2 Electron Microscopy 18
3.2 Run 2 24
3.2.1 Visual Inspection 24
3.2.2 Electron Microscopy 24
3.3 Run 3 28
3.3.1 Visual Inspection 28
3.3.2 Electron Microscopy 30
3.3.3 Comparison 35

4 Conclusion **36**

5 References **37**

Abbreviations

BIB	Broad Ion Beam.
EDX	Energy-dispersive X-ray spectroscopy.
FIB	Focused Ion Beam.
FSS	Ferritic Stainless Steel.
SEM	Scanning Electron Microscopy.
SOFC	Solid Oxide Fuel Cells.

1 Introduction

In the society of today with an ever increasing energy consumption, the demand for renewable and thus sustainable energy sources is getting closer attention every day[1]. But not only should such sources be renewable, also the exhaust and waste products are required to be non-hazardous[2]. Popular candidates which fulfill these demands, such as wind and solar power, however, lack the independence from seasonal changes of the weather or the day-and-night circle[3,4]. In order to overcome this problem, the generated power can be converted into hydrogen[5,6]. Together with the technology of fuel cells, the hydrogen can then be used to generate electrical energy when wind or solar power is not accessible[7]. Furthermore, hydrogen is not the only candidate which can be used for energy generation. Fuel cells have a great fuel flexibility, allowing for example CO or CH_4 to be applied as fuel sources[8]. Furthermore, the high energy efficiency of fuel cells of about 70% - 80% makes them additionally attractive[9]. Lastly, the low and non-toxic emissions are another good reason for an increased interest in the fuel cell technology.

1.1 Fuel Cells

Fuel cells function by generating electrical energy with the electrochemical reaction of a fuel such as hydrogen or natural gas with oxygen. Ambient air contains sufficient oxygen required for this reaction. Both the oxidation of fuel and the reduction of oxygen are separated from each other by an electrolyte. The electrolyte allows ions to diffuse through it, while inhibiting the transport of electrons. Instead, the electrons are transported through an external circuit resulting in electrical current. This can be utilized by inserting a load[7]. The simplest setup of a fuel cell consists of three different parts[10]:

1. The anode where hydrogen or natural gas is oxidized (equation 1).
2. The cathode where oxygen is reduced (equation 2).
3. The electrolyte which electrically separates the two parts and enables the diffusion of O^{2-} ions from cathode to anode side.

The overall reaction (equation 3) is strongly exothermic with a Gibbs free energy of $-228.59\,\mathrm{kJ/mol}$[7].

$$2H_2 \rightarrow 2H^+ + 2e^- \tag{1}$$

$$O_2 + 4e^- \rightarrow 2O^{2-} \tag{2}$$

$$2H_2 + O_2 \rightarrow 2H_2O \tag{3}$$

$$\Delta G^0 = -228.59 \frac{kJ}{mol}$$

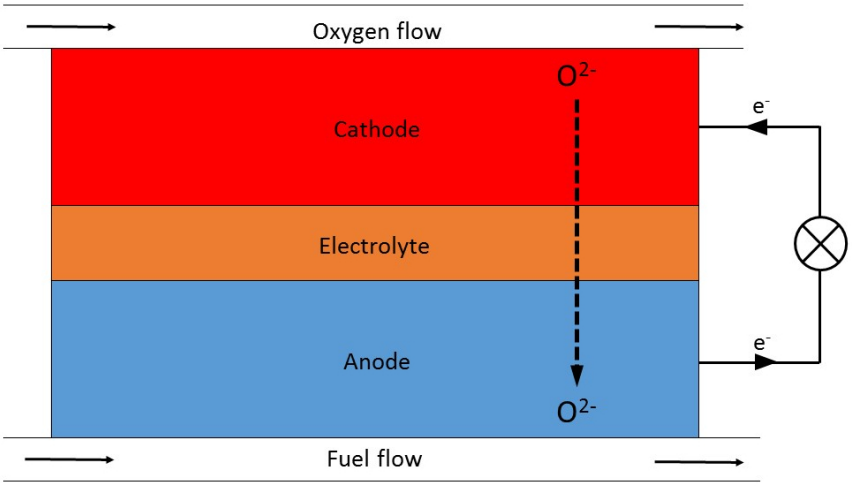


FIGURE 1.1: Sketch of a fuel cell.

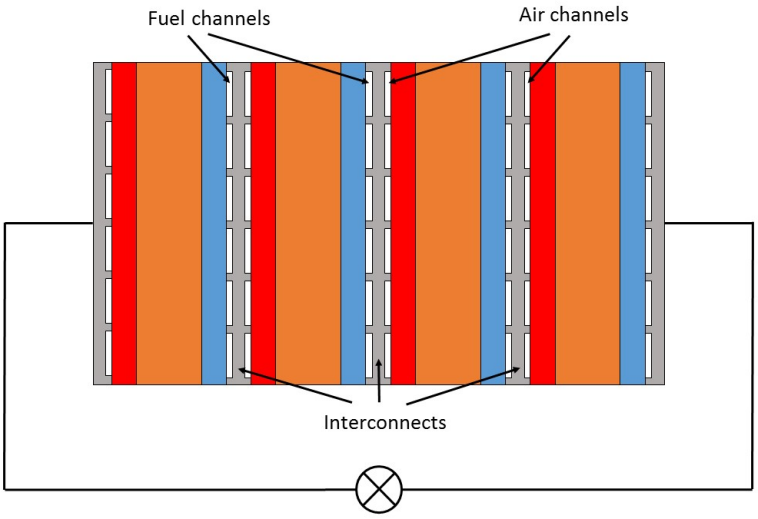


FIGURE 1.2: Sketch of a stack of several single fuel cells.

A general setup of a fuel cell is shown in figure 1.1. Different fuel cell systems exist which are distinguished according to their electrolyte. These electrolytes can for example be polymers, molten carbonate or phosphoric acid[11]. This work however, focuses on another type which works on solid oxide electrolytes. These are therefore called solid oxide fuel cells (SOFC).
Both batteries and fuel cells rely on electrochemical reactions. A major advantage of a fuel cell over a battery is that the chemicals needed for the reaction (hydrogen and air) can theoretically be supplied indefinitely, whereas a battery needs to be recharged after a certain amount of time[12]. This makes fuel cells applicable as stationary backup power units[12] or more recently in mobile applications for example as range extenders[13].
A single fuel cell creates an electric potential below one volt. The exact potential is dependent on parameters such as pressure and temperature as well as on the electrolyte[14]. Since this is not sufficient to power an electrical load, several cells must be electrically connected by interconnects, forming a so called stack (see figure 1.2).

1.2 Interconnect

Interconnects for SOFC need to fulfill several major requirements[11]:

- Low ionic conductivity
- High electrical conductivity
- Chemical stability in SOFC conditions
- A thermal expansion coefficient similar to all other parts of the SOFC
- Impermeability towards the gases used on anode and cathode
- Sufficient mechanical strength

In the past, interconnects were made from ceramics. These, however are very costly and require high working temperatures. Furthermore, ceramics involve difficulties with processing and sintering making their application unfavorable[15]. Apart from ceramics, tailor-made steels such as Crofer 22 APU fulfill the aforementioned requirements. This particular steel, however, is comparably costly which has stimulated the search for alternatives. Thus, steels with coating or the cheaper AISI 441 are getting further attention. Advances in the electrolyte technology allowed for lower operating temperatures of around 600 °C to 900 °C[16]. This enabled the application of ferritic stainless steel (FSS) as interconnects. The main advantage of FSS compared to ceramics is its lower price and easier processability. Furthermore, FSS provides a higher electrical conductivity than ceramics[17]. Besides the advantages, several papers have been published discussing problems with the chemical stability, i.e. corrosion resistance of steel at elevated temperatures in the atmosphere present in SOFC[11,18,19].

1.3 Corrosion

The term corrosion describes the electrochemical degradation of metal. This occurs for example through reaction of metal with oxygen resulting in a metal oxide. This is (for most metals) a thermodynamically spontaneous reaction and will therefore happen continuously, if the steel is not protected[7]. Some metals such as chromium or aluminum form a thin and dense passivating layer of metal oxide on their surface. This layer hinders the reaction of metal and oxygen by inhibiting the oxygen from reaching the unoxidized metal. Thereby, further oxidation is slowed down. Iron, on the other hand, forms a thick, porous and fast growing oxide which thus has little passivating properties[20]. Therefore, the passivation has to be provided by another metal. In steel, this is done by alloying

iron with another metal. It is important that the metal of choice is preferably oxidized compared to the iron.

Typically, high temperature applications add chromium, aluminum or silicon to the alloy, which form respectively chromia (Cr_2O_3), alumina (Al_2O_3) or silica (SiO_2) on the surface and thereby mitigate corrosion[20]. Even though all these oxides form a thin and dense passivating layer, alumina and silica exhibit high electrical resistance. Therefore, alloys containing elevated amounts of Al or Si are not suitable candidates as SOFC interconnects[21]. The high temperature corrosion protection has to be provided by the more conductive chromia[10]. The underlying mechanism will be further explained in chapter 1.3.1.

As already mentioned, the oxide former has to be oxidized preferentially in order to protect the steel. This thermodynamic process can be visualized with the Ellingham-diagram (see figure 1.3).

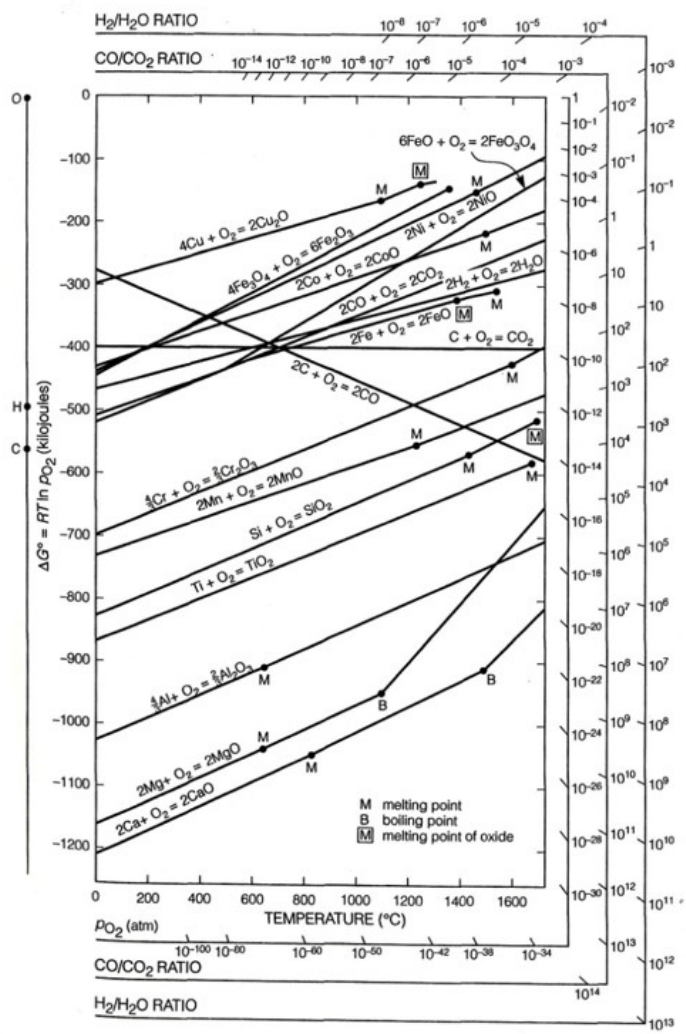


FIGURE 1.3: Ellingham diagram for several metals and their respective oxides[22].

The Ellingham-diagram depicts the stability of metal oxides under certain circumstances. The curves in figure 1.3 are calculated using the Gibb's free energy (see equation 4) according to equation 5.

$$\Delta G = \Delta H - T\Delta S \tag{4}$$

$$\Delta G = \Delta G^0 + RTlnQ \tag{5}$$

G^0 in this equation represents the free energy under standard conditions and Q describes the reaction quotient. For a reaction of a metal M with oxygen (equation 6) the quotient can be calculated using equation 7, where $a()$ represents the activity of the species.

$$xM + \frac{y}{2}O_2 \leftrightarrow M_xO_y \tag{6}$$

$$Q = \frac{a(M_xO_y)}{a(M)^x a(O_2)^{\frac{y}{2}}} \tag{7}$$

As both the metal and its oxide are found in their solid state, their activities can be approximated with $a = 1$. Also, for equilibrium conditions, ΔG must be zero. This results, using equations 5 and 7, in the following expression:

$$\Delta G^0 = -RTln\Big(\frac{1}{a(O_2)^{\frac{y}{2}}}\Big) \tag{8}$$

The activity of oxygen can be approximated by its partial pressure, resulting in equation 9.

$$p_{O_2} = \exp\Big(\frac{1}{y} \cdot \frac{2\Delta G^0}{RT}\Big) \tag{9}$$

This relation is shown in the Ellingham-diagram for several metals. With the help of the diagram it is possible to determine whether the metal is stable under the present conditions or its respective oxide[20,23]. In a fuel cell the partial pressure of O_2 on the fuel side is approximately 10^{-22} to 10^{-16} Pa[24]. According to the Ellingham-diagram at 600 °C to 800 °C, FeO and Cr_2O_3 are thermodynamically stable under these pressures. However, Cr_2O_3 will be preferentially oxidized and thus form a protective oxide layer on the surface of the steel.

1.3.1 Corrosion Protection

Apart from kinetic aspects, however, the Ellingham-diagram shows that under the given atmosphere in fuel cells, several forms of iron oxide are thermodynamically stable. Iron oxide grown in humid air is reported to be porous and fast growing and therefore requires a thick oxide layer in order to impede further oxidation[25]. In fuel cells, a thick scale leads to mechanical stresses due to the mass gain and the inherent change in volume of the interconnect. Furthermore, the growth of iron oxide leads to a decline in conductivity decreasing the overall performance of the interconnect and thus the fuel cell. Therefore, chromium is added to the alloy to hinder the oxidation of iron.
The oxidation of a metal can be divided into three consecutive steps[20]:

1. The adsorption of gaseous oxygen onto the metal surface (figure 1.4 (a)).
2. The nucleation of oxides and lateral growth until the formation of a continuous oxide layer (figure 1.4 (b)).
3. The thickening of the oxide layer on the surface (figure 1.4 (c)).

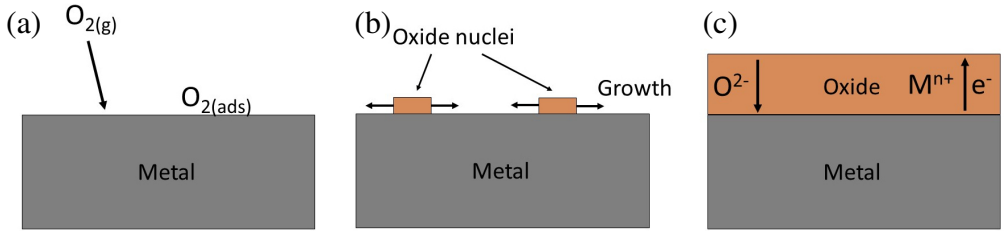


FIGURE 1.4: The three steps of an oxide growth: adsorption of oxygen (a), lateral growth of oxide (b), increase of the oxide's thickness (c)[23].

Further oxidation after step 1 and 2 is diffusion controlled by the rate of either inward diffusion of O^{2-} or outward diffusion of M^{n+} species. Therefore, the growth speed and growth direction is dependent on the diffusion rate of these two species. Oxides are often classified by their semiconductor properties[26]. That means the predominant defect type determines whether the oxide is an n-type or a p-type oxide:

- Metal excess
- Anion vacancy

} n-type semiconductor

- Oxygen excess
- Cation vacancy

} p-type semiconductor

Since metals in an oxide are positively charged, an excess of them requires additional electrons in order to ensure charge neutrality. The same is true for a lack of anions (oxygen in the case of an oxide). Oxides with these predominant defect types can therefore be classified as n-type semi-conductors as both cases require additional electrons for charge neutrality[23]. Respectively, an excess of oxygen or a lack of metal cations results in a p-type semiconductor[3].
Depending on the predominant defect type in the oxide, its growth can either be inward or outward growing. If the oxygen defects dominate the defect structure, the oxide is inward growing, since oxygen can then be transported through the oxide towards the metal-oxide interface. A surplus of metal defects in the lattice leads to an outward growing oxide by outward diffusion of metal-ions through the oxide[23]. This transport of ions is driven by the electrical potential of the reduction of oxygen and the oxidation of the metal. In order to prevent further oxidation of the metal, a dense oxide layer covering the entire metal surface is necessary. This oxide works as a barrier against the diffusion of ions[23].
Previous work on chromium oxide has shown that it contains cation vacancies at high oxygen partial pressure and metal excess at low oxygen partial pressure[27]. In both cases, the metal ion is the predominant defect which means the growth direction of the oxide is outward[28]. Protection of an interconnect against corrosion is achieved by formation of a continuous chromium oxide layer on the surface of the metal. To ensure this the amount of chromium in the alloy has to be sufficiently high: values in the literature range from 17wt% to 25wt% to prevent oxide spallation or internal oxidation[9,21]. Lower Cr content has been shown to decrease the corrosion stability of the interconnect. If the amount of chromium is not sufficient for providing a uniform Cr_2O_3 scale, iron rich oxide nodules appear on the surface. This process is called breakaway corrosion. However, even if sufficient Cr is present in the alloy in the first place, breakaway corrosion can appear if the amount of chromium on the surface is diminished by evaporation. If the evaporation is faster than the resupply of Cr from the alloy, the oxide breaks down causing breakaway corrosion[17].

1.3.2 Chromium Evaporation

A number of papers have been published concerning the process of chromium evaporation i.e. the formation of volatile hexavalent chromium species[19,23,29,30]. This happens due to the reaction of Cr_2O_3 and oxygen under humid conditions according to equation 10. The associated decrease in oxide thickness leads to a faster oxidation of chromium from the oxide which exhausts the alloy of chromium.

$$Cr_2O_{3(s)} + \frac{3}{2}O_{2(g)} + 2H_2O_{(g)} \rightarrow 2CrO_2(OH)_{2(g)} \quad (10)$$

If the protection by chromia cannot be ensured anymore, the alloy underneath corrodes. This happens via the formation of hematite (Fe_2O_3) nodules that appear on the steel surface and subsequently spread over the entire surface[18,31]. These nodules are outward growing by outward diffusion of iron, leaving a porous structure behind. This porosity and the high growth speed of the hematite leads to reduced conductivity and degradation of mechanical strength and hence corrupts the integrity of the steel as an interconnect[18].

1.4 Influence of Surface Conditions

It has been shown that the surface structure influences the corrosion resistance. In the present work the surface of the samples was mechanically altered by grinding or polishing, before and after pre-oxidation. It is important to note that this kind of treatment introduces defects into the surface which increase the overall entropy of the surface. Whether this influences the oxidation behaviour positively, negatively or not at all has been investigated by *Ostwald et al.* and *Niewolak et al*[32,33]. The results are shown in figure 1.5.
Ostwald et al. investigated the growth rate of the oxide layer of 20%Cr-32%Ni steel at 600 °C in different atmospheres (see figure 1.5 (a)). After 100 h exposure, it appears to be dependent on the quality of the sample surface - the higher the deformation the faster the oxide growth. Higher deformation was present for sandblasted samples compared to the polished samples. After exposure for 1000 h however (figure 1.5 (b)), the reduced growth speed appears to hinder the oxide from becoming sufficiently protective, as shown by *Niewolak et al.* Here, fast growing iron oxide was found for the sample polished to 1 µm surface finish.
The results of the two experiments are contradictory to each other regarding surface quality dependent growth speed. It is possible to conclude that the different surface conditions affect the oxidation characteristics, however it is hard to predict under which circumstances the oxidation is accelerated or slowed down.

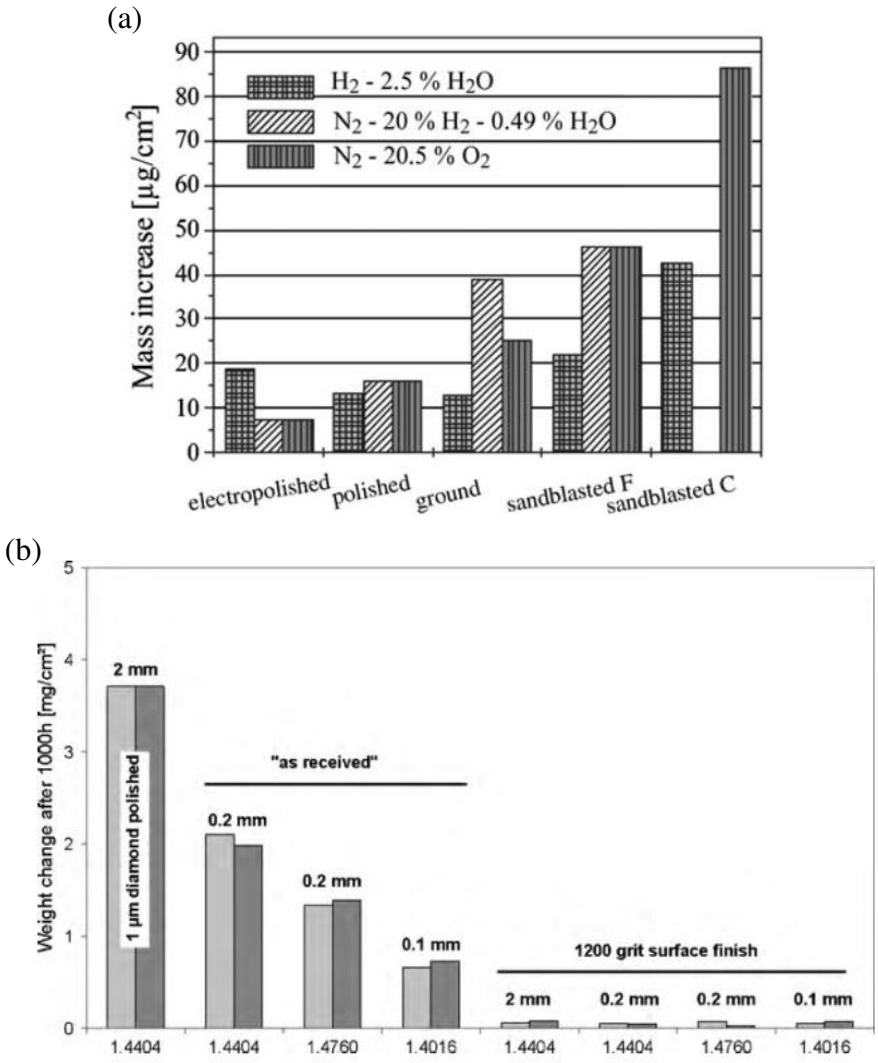


FIGURE 1.5: Investigation of mass gain of steel for different surface finishes: (a) Mass gain of 20%Cr–32%Ni steel with different surface treatments and atmospheres exposed at 600 °C for 100 h[32]; (b) Mass gain of different steels with different surface finishes that were exposed at 600 °C for 1000 h to humid 4%H_2 - 96% Ar[33].

1.5 Dual Atmosphere and Inverse Temperature Effect

Already in 2004 *Yang et al.*[31] compared chromia forming steel samples exposed to air only, hydrogen only, or dual atmosphere at 800 °C and 850 °C. It was found that samples exposed to dual atmosphere show hematite nodules whereas single atmosphere exposed samples did not. This suggested that the reason for the faster corrosion of the samples exposed to dual atmosphere is the diffusion of hydrogen through the steel. According to *Yang et al.*, its presence in the oxide accelerates the outward transport of iron and thus leads to breakaway corrosion.

A similar study at lower temperature (600 °C) was done by *Alnegren et al.* in 2015[18]. Here, samples were exposed to humid air on both sides, and simultaneously other samples were exposed to dual atmosphere conditions. All samples were pre-oxidized for 3 hours at 800 °C prior to exposure to replicate the sintering of the fuel cell during production. These pre-oxidation parameters result in a Cr_2O_3 layer of about 140 nm in thickness. After 1000 hours of exposure the samples exposed to dual atmosphere showed a thick oxide while those exposed only to air on both sides still exhibited protective behaviour. This suggests that the previously mentioned chromium evaporation is not the only factor leading to the degradation of interconnects which is consistent with the study conducted by *Yang et al.*[31].

Another work by *Alnegren et al.*[34] investigated the temperature dependency of the dual atmosphere effect. The results are shown in figure 1.6. At 800 °C in both dual and single atmosphere (figure 1.6 (c) and (f)) the samples exhibit continuous chromium oxide although it has spalled off at the edge of the sample during cooling after exposure. The composition of the protective oxide layer was confirmed by EDX analysis to be thick Cr_2O_3. At 700 °C (figure 1.6 (b) and (e)) the surface is intact without any form of spallation or breakaway corrosion. However, the exposure at 600 °C led to severe corrosion in dual atmosphere (figure 1.6 (d)), compared to single atmosphere (figure 1.6 (a)). Since this behaviour contradicts what is commonly found, this is called inverse temperature effect. The mechanism behind it is not yet fully understood.

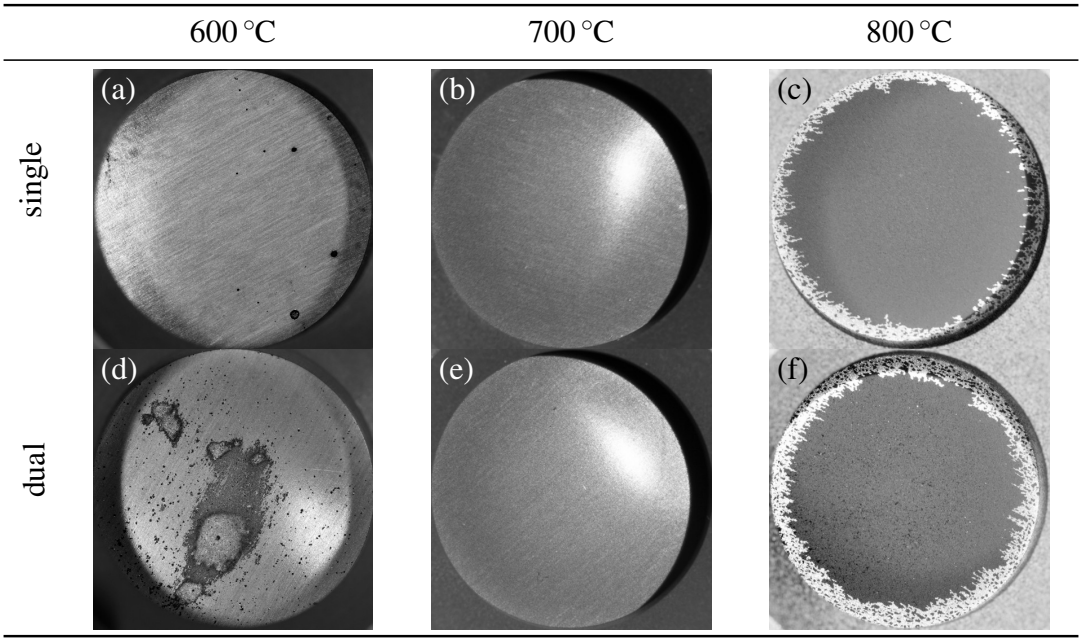


FIGURE 1.6: Results from *Alnegren et al.* on the influence of temperature on dual atmosphere corrosion[34]: (a), (b) and (c) exposed to air on both sides at 600 °C, 700 °C and 800 °C respectively; (d), (e) and (f) exposed to dual atmosphere at 600 °C, 700 °C and 800 °C respectively. The exposure was conducted for 1000 h and the figures show the air side of the samples.

Additional studies have shown that pre-oxidation of the samples migitates the onset of breakaway corrosion[24,31]. A recent investigation on the effect of pre-oxidation time has concluded, that longer times help extending the interconnects' life time[35]. This finding might enable accelerated testing for research purposes as done in this work. Whether the beneficial effect of pre-oxidation is due to reduced hydrogen transport from the anode side or the formation of a protective oxide on the cathode side has not been investigated.

1.6 Aim

The aim of this project is to better understand the underlying mechanism that leads to corrosion under dual atmosphere conditions. As mentioned before, previous work has shown that the thickness of the passivating Cr_2O_3 layer has a positive influence on the performance of the material. What has not yet been investigated is whether the protection of the air side or the protection of the hydrogen side is more important. An answer to this question might help for future SOFC applications to increase the lifetime through application of a coating on the critical side of the interconnect.

2 Experimental

2.1 Samples

The steel utilized, AISI 441, is 0.3 mm thick with a chemical composition as stated in table 2.1. The steel had been rolled during production and the the samples were prepared according to figure 2.1 as received.

TABLE 2.1: Chemical composition of AISI 441 in weight%.

Cr	Si	Nb	Mn	Ni	Ti	P	N	C	S	Fe
17.56	0.59	0.39	0.35	0.26	0.173	0.03	0.017	0.014	0.001	balance

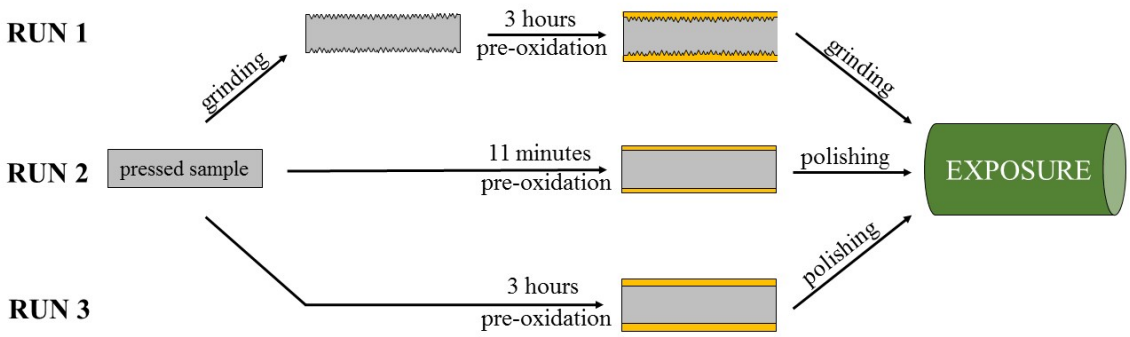


FIGURE 2.1: Schematic preparation path of the samples for the different runs.

First, the steel was pressed out with a hydraulic press into circular samples with a diameter of 21 mm. These were then cleaned in an ultrasonic bath for ten minutes in acetone and ethanol subsequently. In order to get more reproducible data, the samples of run 1 were ground prior to the pre-oxidation. However, this could affect the oxidation characteristics as discussed in chapter 1.4. That is why for run 2 and 3 the samples were not ground before the pre-oxidation. After cleaning, the samples were pre-oxidized at 800 °C in a tubular furnace under a stream of ambient air. The air flow was set to 280 sml/min with 3% H_2O. The respective times of pre-oxidation are shown in table 2.2. By varying the pre-oxidation time, different thicknesses of protective oxide layer were achieved.

Since the premise of this work was to investigate whether air side or hydrogen side protection is more decisive for the interconnect lifetime, the oxide layer was mechanically removed according to table 2.2. This was done using 1200 grit SiC-paper. Samples for run 2 and 3 were further polished with diamond paste up to 1 µm.

TABLE 2.2: The table shows which pro-oxidation layers were removed after the pre-oxidation prior to exposure.

	pre-oxidation	Surface	Sample 1	Sample 2	Sample 3 & 4	Sample 5 & 6
Run 1	3h	ground	none	none	cathode	anode
Run 2	11min	polished	both	none	cathode	anode
Run 3	3h	polished	both	none	cathode	anode

2.2 Experimental setup

The samples were placed into the sample holder (see figure 2.2).

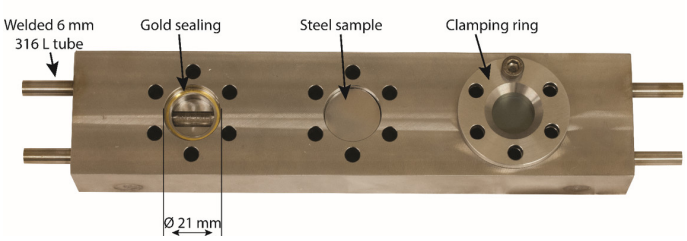


FIGURE 2.2: Sample holder used for the dual atmosphere exposure.

Six samples were placed into the holder at the same time; three on each side. Two channels led through the core of the holder providing humid hydrogen to the backside of the sample. The air supply was provided outside the holder through the tubular furnace. The samples were fixated onto the holder with clamping rings. Gold rings between sample and holder ensured gas tightness.
The exposure was conducted at 600 °C in dual atmosphere, simulating the conditions in a SOFC. 3% humidity was achieved by bubbling the gas through a warm water bath connected to a condenser set to 24.4 °C. The exact composition of the two gases used, hydrogen and air is shown in table 2.3.

TABLE 2.3: Exposure atmospheres

	Atmosphere	Flow rate
Hydrogen side	Ar - 5% H_2 - 3%H_2O	100 sml/min
Air side	Air - 3%H_2O	8800 sml/min

The furnace was heated and cooled with a rate of 1 °C/min in order to prevent spallation of the oxide layer due to thermal stresses. The exposure was interrupted after certain time intervals to visualize the progression of the breakaway corrosion by camera. This is schematically shown for run 1 in figure 2.3 and for all runs in table 2.4. At the end of the exposure another set of pictures was taken and afterwards, the samples were removed from the holder. Then, they could be investigated with electron microscopy and EDX (top view and cross-sections) which will be described in chapter 2.4.

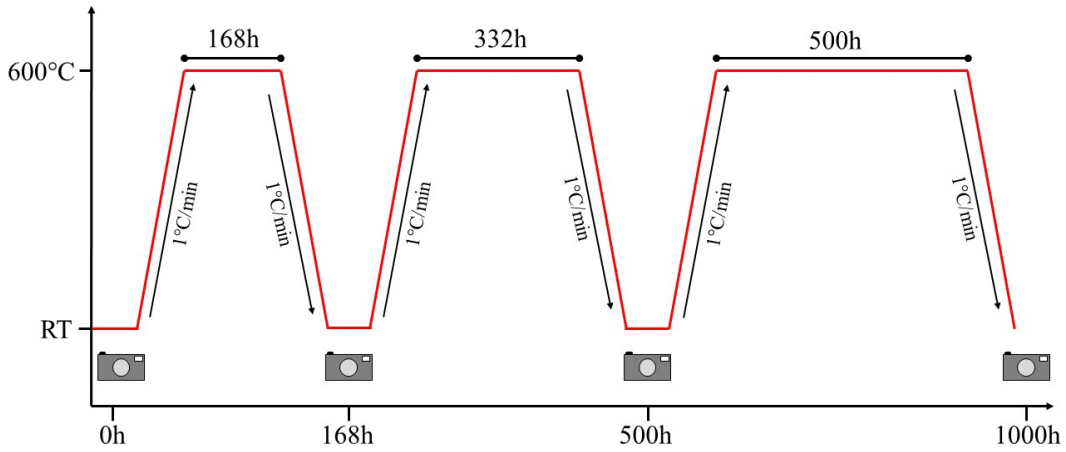


FIGURE 2.3: Temperature profile of run 1.

TABLE 2.4: Duration of exposures

	Break	Break	Termination
Run 1	168 h	500 h	1000 h
Run 2		24 h	168 h
Run 3			500 h

2.3 Analytical Methods

2.3.1 Cross-section Preparation

In order to investigate cross-sections, the samples were cut with a low speed saw. A piece of a silicon wafer was then glued onto the sample to protect the oxide from the subsequent ion milling. The cross-section of the samples was then polished and the sample was mounted into a Leica EM TIC 3X bread ion beam BIB system (see figure 2.4). The available BIB operated using a Gallium source and an acceleration voltage of 6.5 kV was applied. The resulting smooth surface could then be analysed with electron microscopy.

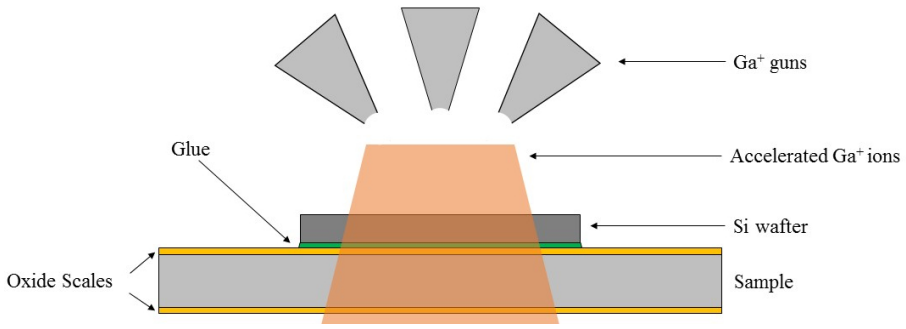


FIGURE 2.4: Schematic setup of the broad ion beam milling.

In order to acquire information on a selected area of one sample, it was prepared using focused ion beam (FIB) milling (FEI Versa3D LoVac DualBeam). The FIB works similar to the BIB, however the ion beam is highly focused. That means a small area of the sample can be milled by the ion beam. The thus prepared samples could then be investigated with electron microscopy.

2.4 Microscopy Analysis

When high energy electrons interact with atoms, electrons can be released from one of the atoms' shells. This creates secondary electrons as shown in figure 2.5 (a). The low energy of these electrons leads to a high surface sensitivity. Depending on the angle between incoming beam and surface of the sample the amount of secondary electrons can increase or decrease. This creates contrast in the intensity on the detector which can therefore be used to analyze sample topography[36].

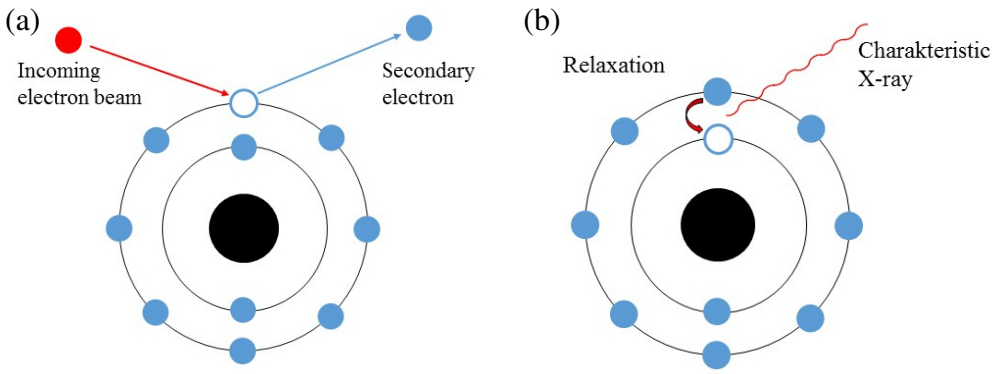


FIGURE 2.5: The two forms of interaction analysed with scanning electron microscopy: (a) creation of a secondary electron, (b) relaxation of an excited atom and the subsequent creation of a characteristic X-ray[36].

After an electron from an inner shell of an atom has been released by the incoming beam, the atom is in a meta-stable excited state (see figure 2.5 (b)). An electron from a higher shell will eventually relax into the lower energy shell and the consequent energy will be released by X-ray photons. Since the distances between electron shells of all elements are distinct, this radiation is a fingerprint for every element and can be used for chemical analysis[36].

X-rays are less likely to interact with matter which leads to a much larger interaction volume compared to secondary electrons as shown in figure 2.6. As a result, EDX exhibits a lower surface sensitivity[36].

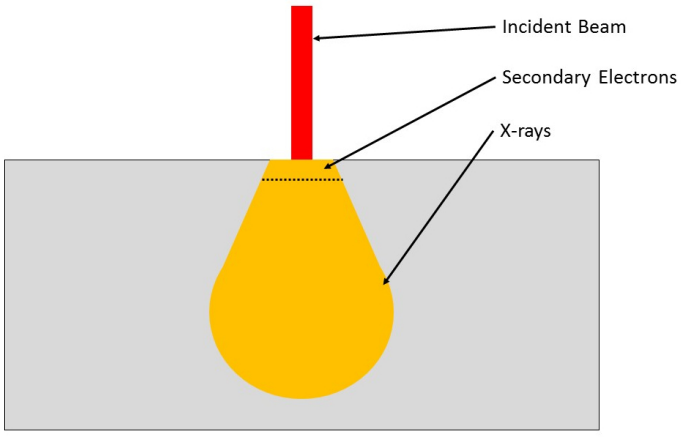


FIGURE 2.6: Interaction volume of secondary electrons and X-rays for electron microscopy[36].

3 Results and Discussion

3.1 Run 1

3.1.1 Visual Inspection

All pictures taken of run 1 throughout exposure can be seen in figure 3.1. As only little breakaway corrosion is visible after 168 hours and 500 hours the exposure was continued until 1000 hours. After 1000 hours small nodules which were suspected to be iron oxide were visible on the air facing side of the samples. These nodules appear on all samples with the exception of sample 1.4. Subsequent SEM investigations were done on samples 1.1, 1.3 and 1.6 (see figure 3.2).

3.1.2 Electron Microscopy

Figure 3.2 shows secondary electron microscopy images after exposure. The entire surface of the steel samples shows nodules. EDX was performed on all samples shown in figure 3.2. The EDX result of sample 1.1 is shown in figure 3.3 and corresponding table 3.1 and is respective for all other samples.

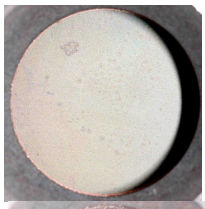
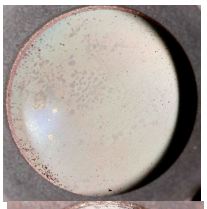
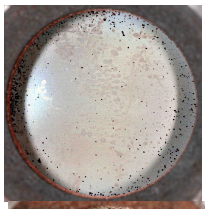
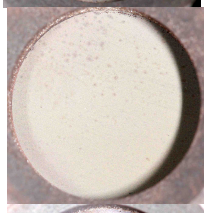
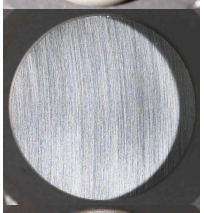
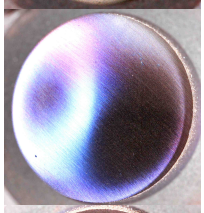
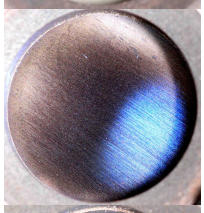
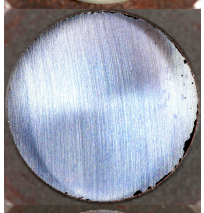
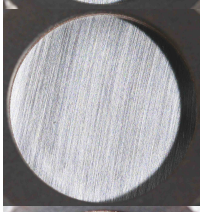
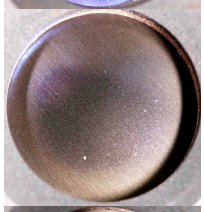
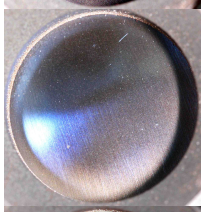
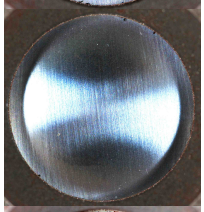
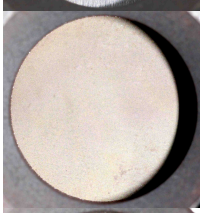
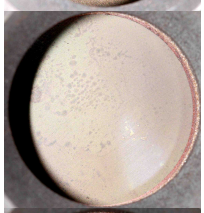
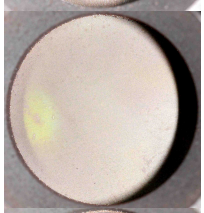
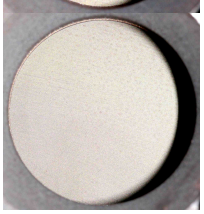
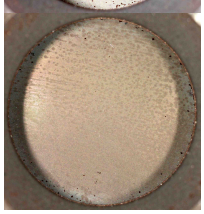
Sample	0 hours	168 hours	500 hours	1000 hours
1.1 Oxide on both sides				
1.2 Oxide on both sides				
1.3 Oxide on anode side				
1.4 Oxide on anode side				
1.5 Oxide on cathod side				
1.6 Oxide on cathode side				

FIGURE 3.1: Photographs taken of run 1. The samples were exposed in dual atmosphere at 600 °C for 168 h, 500 h and 1000 h respectively. The samples were pre-oxidized at 800 °C for 3 h. The protective layer was ground off prior to exposure on the air facing side of sample 1.3 and 1.4 and the hydrogen facing side of sample 1.5 and 1.6.

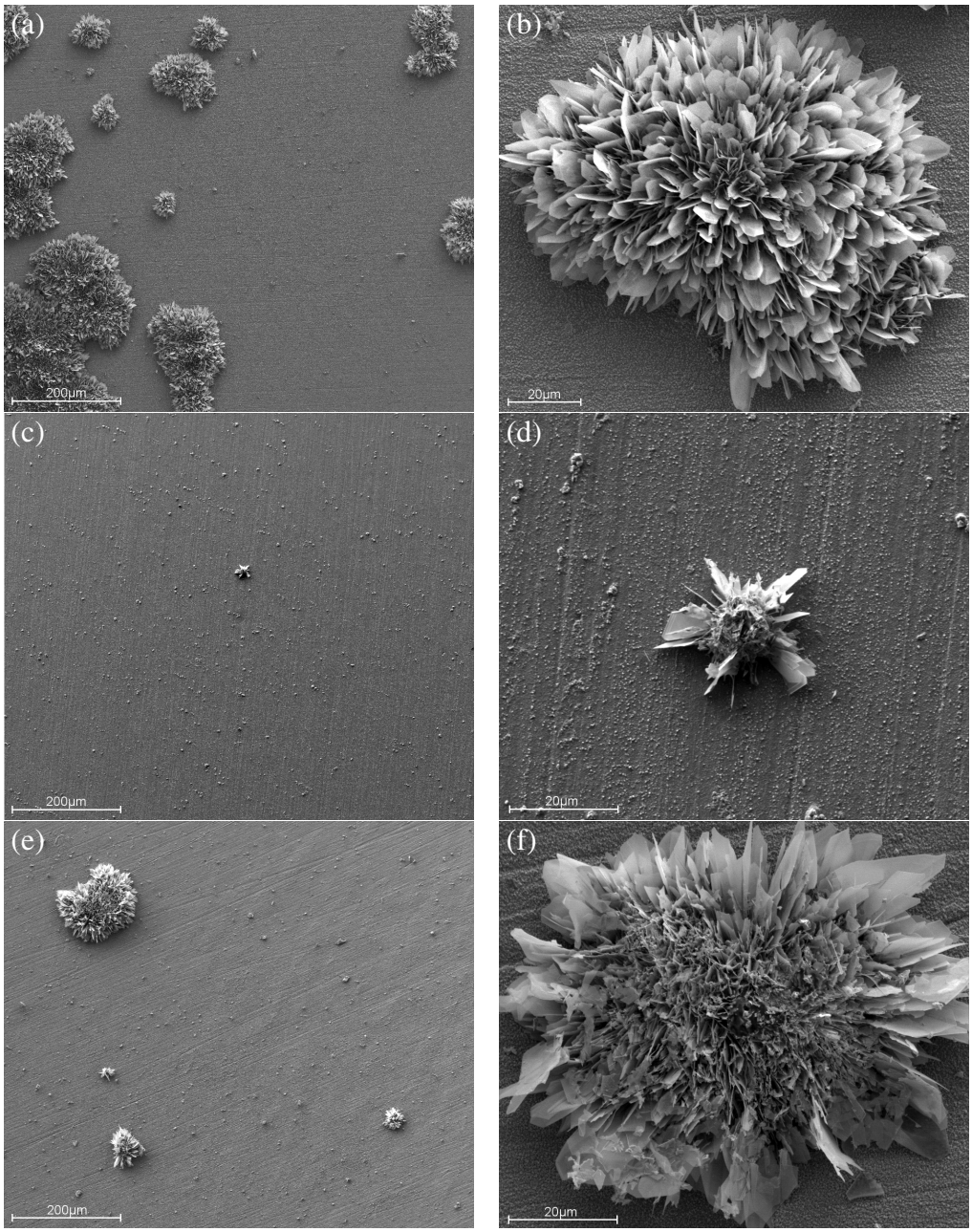


FIGURE 3.2: SEM images recorded on the air facing side of samples from run 1. (a) and (b): sample 1.1 (oxide on both sides), (c) and (d): sample 1.3 (oxide on hydrogen side), (e) and (f): sample 1.6 (oxide on air side). The samples were exposed in dual atmosphere at 600 °C for 1000 h.

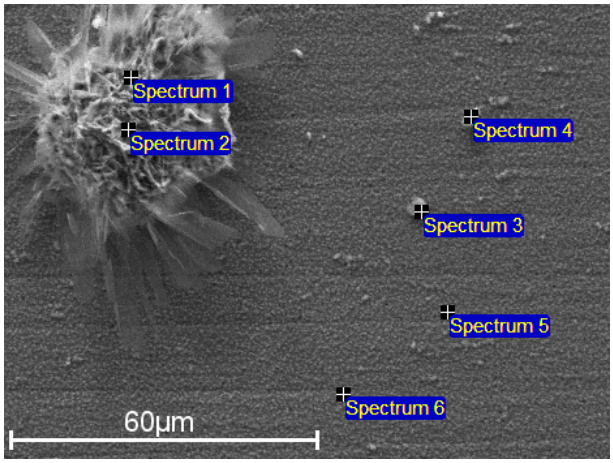


FIGURE 3.3: Locations of EDX spectra recorded on the air facing side of sample 1.1 (oxide on both sides). The sample was exposed in dual atmosphere at 600 °C for 1000 h. The corresponding EDX results are shown in table 3.1.

TABLE 3.1: EDX results of the spots of sample 1.1 in figure 3.3. The values are given in atomic% and rounded. The spectra are recorded on a nodule (1 and 2), surface anomalies (3 and 4) and the plain surface (5 and 6). The sample was exposed in dual atmosphere at 600 °C for 1000 h.

Spectrum	O	Al	Si	Ti	Cr	Mn	Fe	Ni	Cu	Nb
1	51		0.1		7.7	0.3	40			
2	65	0.5	0.1		5.3	0.2	29			
3	49	0.2	2.5	0.5	16	2.0	24	5.1		0.1
4	56	0.8	0.4	0.3	5.3	1.2	36		0.2	
5	21	0.2	1.1	0.4	16	1.1	60			0.1
6	33	0.3	1.2	0.7	16	3.2	46		0.1	0.2

Spectrum 1 and 2 were recorded on one of the nodules, which have been observed before and were proven to be iron oxide in previous work[9,17,18,31]. The EDX performed here, indeed showed an elevated oxygen content compared to the other spectra. Together with the low chromium content here, this confirms the presence of iron oxide. Similar values were found in spectrum 4 which was recorded on a small surface abnormality. Spectrum 3 which was also recorded on a small bright spot shows an elevated amount of Ni. Spectrum 5 and 6 both were recorded on the surface which covered most of the sample. Due to the high chromium content in these spectra, it can be concluded that the sample is covered by a layer of chromium oxide.

The cross-section of sample 1.6 was investigated and is shown in figure 3.4. The protective chromium oxide scale is visible in (a) and a nodule in (b). To determine the nodule's composition, an EDX mapping was recorded here, which is shown in figure 3.5. The EDX shows that the upper part of the nodule consists of iron (figure 3.5 (b)) and oxygen (figure 3.5 (d)) and hardly any chromium (figure 3.5 (c)), resulting in iron oxide. Furthermore, the area below the nodule, contains an elevated amount of oxygen as well, with a slight increase in the chromium signal compared to the bulk. This means that the upper part of the nodule grew outwards whereas the area underneath appeared due to inward growth.
In order to determine which of the samples is most prone to corrosion, the results of run 1 are not sufficient. However, a small indicator might be taken from SEM analysis. The topview pictures on the left side of figure 3.2 show that compared to sample 1.3 and 1.6, sample 1.1 (figure 3.2 (a)) appears to be covered the most by iron oxide nodules. Despite that, the differences are rather small and therefore, make ranking the samples impossible. Furthermore, sample 1.1 which appears to be most corroded has protective oxide on both sides by Cr_2O_3. This is contradictory to what has been found in previous work[17–19,30,37]. The reason for this discrepancy might come from surface effects due to the grinding as discussed in chapter 1.4.
In order to decrease the influence of the surface and to avoid the corrosion of all samples, the experiment was repeated with different parameters.

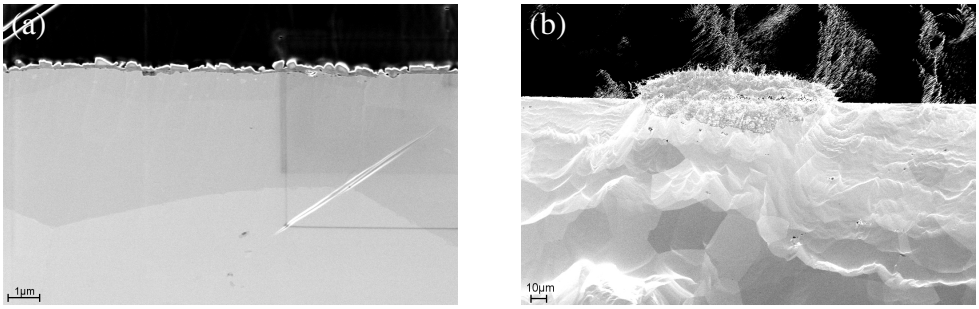


FIGURE 3.4: Cross-section of sample 1.6. The images were recorded on the air facing side after 1000 h exposure in dual atmosphere at 600 °C. (a) protective chromium oxide scale; (b) iron oxide nodule.

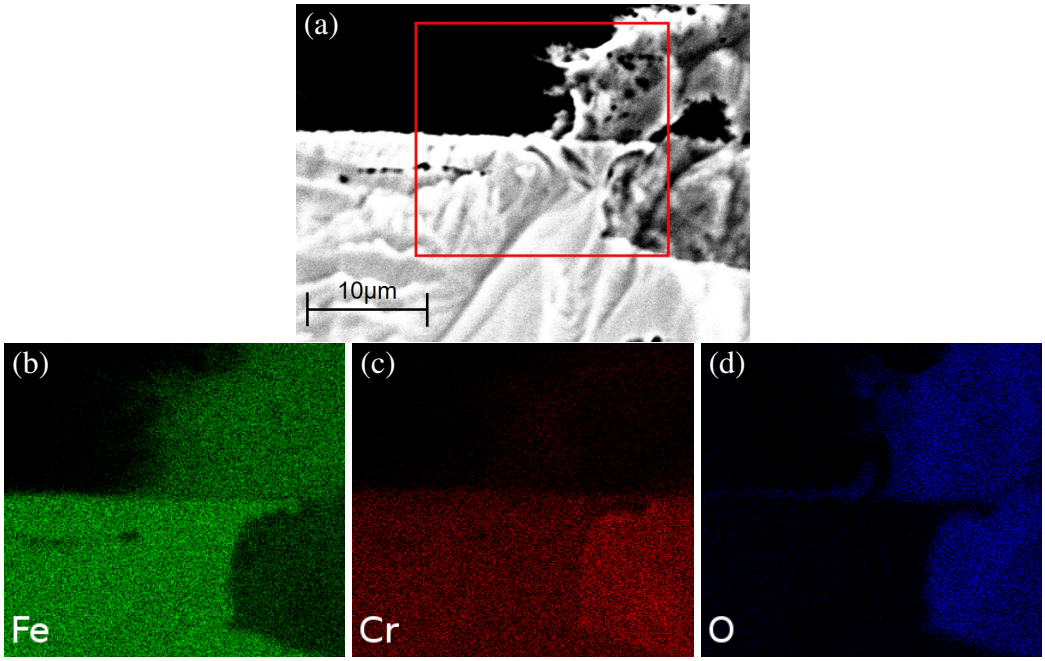


FIGURE 3.5: EDX mapping as recorded on a nodule in the cross-section of sample 1.6. (a) shows the electron image, (b) Fe, (c) Cr and (d) O signal. The sample was exposed in dual atmosphere at 600 °C for 1000 h.

3.2 Run 2

3.2.1 Visual Inspection

The exposure of run 2 was interrupted after 24 hours but no breakaway corrosion was visible. After 168 hours exposure, however, breakaway corrosion is present in all samples. It appears to be most severe on sample 2.1 which was expected, as it had no protective oxide prior to exposure. Also samples 2.3 and 2.4 (oxide on hydrogen side) appear to be severely corroded. However in comparison to sample 2.6 (oxide on air side) this is hard to evaluate. Sample 2.2 (oxide on both sides) and sample 2.5 (oxide on air side) seem to show the highest resistance toward corrosion.

3.2.2 Electron Microscopy

Both the failure of sample 2.1 and the resistance of sample 2.2 are already visible from the photographs which is why SEM investigations were only conducted on sample 2.3 (oxide on hydrogen side) and sample 2.6 (oxide on air side). The results are presented in figure 3.7 and 3.8 respectively.

Figure 3.7 (a) depicts the topview micrograph of sample 2.3 with the oxide removed from the air facing side. The nodules in the top left corner appear to have a different shape compared to those in the bottom right corner. A closeup view of the nodules in the top left corner is shown in figure 3.7 (b). The edge of these nodules is flat indicating lateral growth.
The nodules of sample 2.6, however, exhibit rounder edges in figure 3.8. Notably here is their appearance in straight and parallel lines as it can be seen in figure 3.8 (c). This could be an artifact from the steel during production, however this has not been further investigated in the present work.
Both sample 2.3 and 2.6 are severely corroded and no large areas without breakaway corrosion are visible. The same is true for their corresponding samples 2.4 and 2.5. This again makes a conclusion, regarding if air side or hydrogen side protection is more important, impossible.

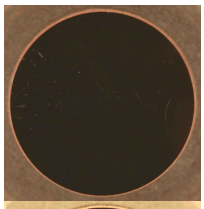
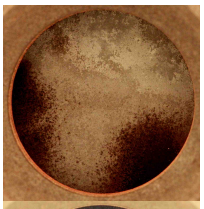
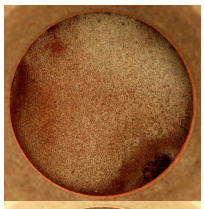
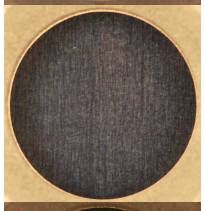
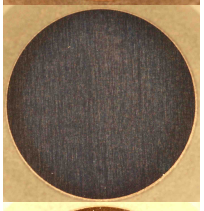
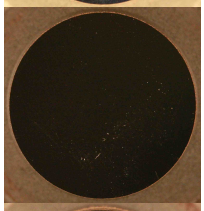
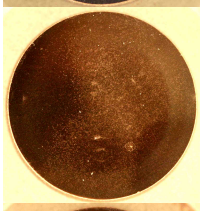
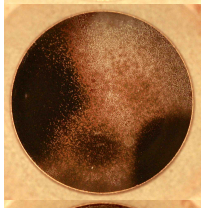
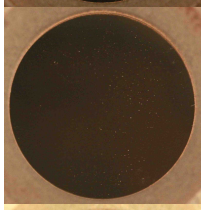
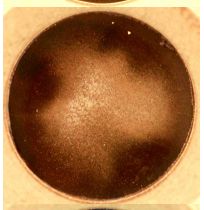
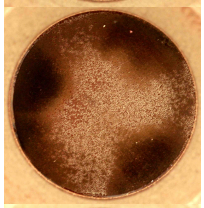
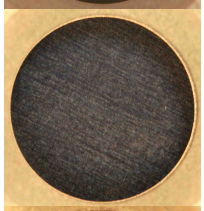
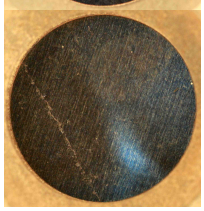
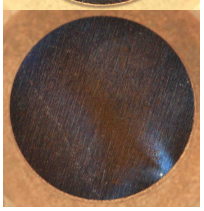
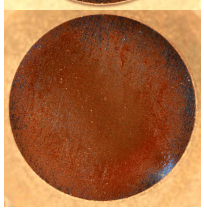
Sample	0 hours	24 hours	168 hours
2.1 Oxide on no side			
2.2 Oxide on both sides			
2.3 Oxide on anode side			
2.4 Oxide on anode side			
2.5 Oxide on cathode side			
2.6 Oxide on cathode side			

FIGURE 3.6: Photographs taken of run 2. The samples were exposed in dual atmosphere at 600 °C for 24 h and 168 h respectively. The protective layer was ground off prior to exposure on both sides of sample 2.1, the air facing side of sample 2.3 and 2.4 and the hydrogen facing side of sample 2.5 and 2.6. The samples were pre-oxidized at 800 °C for 11 min.

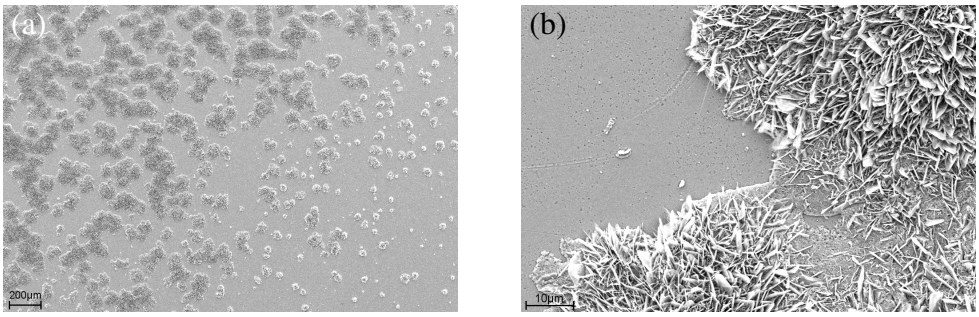


FIGURE 3.7: SEM images taken of the air facing side of sample 2.3 (oxide on hydrogen side). The sample was exposed for 168 h in dual atmosphere at 600 h.

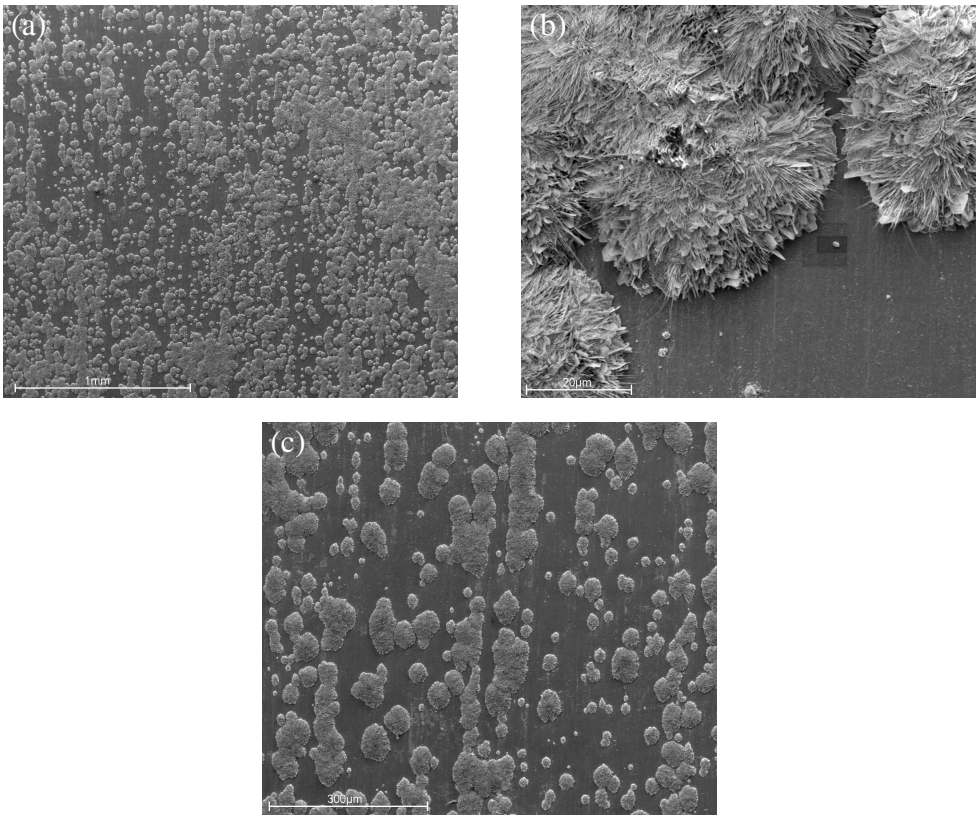


FIGURE 3.8: SEM images taken of the air side of sample 2.6 (oxide on air side). The sample was exposed in dual atmosphere at 600 °C for 168 h.

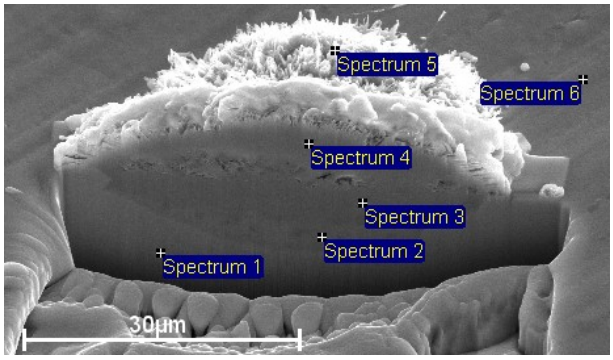


FIGURE 3.9: A nodule of sample 2.5 (oxide on hydrogen side) after FIB milling was conducted here. Subsequent EDX investigation was performed on the indicated sites. The corresponding results are shown in table 3.2. The sample was exposed in dual atmosphere at 600 °C for 168 h.

TABLE 3.2: EDX results of sample 2.5 corresponding to the spots as shown in figure 3.9. The values are given in atomic% and rounded. The sample was exposed in dual atmosphere at 600 °C for 168 h.

Spectrum	O	Si	Cr	Mn	Fe	Ga	Zr
1	8.3		22		66	3.4	
2	16		24	1	57	2.7	
3	23		25		49	2.5	
4	16		5.8		76	2.1	
5	70		1.2		27	1.1	0.4
6		2.5	18		78	1.0	

A nodule of sample 2.5 (oxide on air side) was prepared with FIB to gather further information on the composition of the nodules. The result is shown in figure 3.9 and table 3.2. The gallium content appears due to milling with a Ga source. Furthermore, the nodule was protected with a layer of platinum prior to milling.

Due to the geometry of the trench around the recorded spectra, the values in the table are not very precise. They can therefore only be used as a rough indicator about the major components.

Spectrum 1 was recorded inside the alloy which is why the oxygen content is low here. Spectrum 2 and 3 are located where the nodule exhibits inward growth. Typically, this happens by the formation of $(Fe,Cr)_3O_4$ which can be confirmed by the EDX analysis. The location of spectrum 4 and 5 is in the upper part of the nodule where outward growth of Fe_2O_3 is expected to be found. The EDX shows a high amount of either Fe or O here, which can confirm the presence of iron oxide. Spectrum 6 was recorded on the surface next to the nodule. The lack of oxygen here is measured due to a high penetration of the EDX signal and therefore a strong signal of the underlying alloy. Here, the recorded values are in the range of the pure alloy.

3.3 Run 3

3.3.1 Visual Inspection

The photographs of the third run taken before and after exposure are shown in figure 3.10. After 500 hours sample 3.1 (no oxide on either side) was covered by a thick layer of iron oxide. The protective oxide of Sample 3.2 (oxide on both sides) is mainly intact but shows local breakaway corrosion, however, the visible nodules are scarce and small. Sample 3.3 and 3.4 (oxide on hydrogen side) exhibit limited breakaway corrosion on the edges, however the center of both samples still shows an intact protective oxide layer similar to before exposure. In contrast, sample 3.5 and 3.6 (oxide on air side) are covered by a thick layer of iron oxide. Additionally, spallation of the iron oxide occurs here. In order to confirm the characteristics seen with the naked eye, electron microscopy is performed.

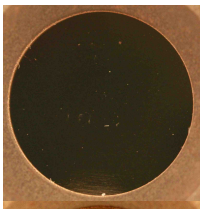
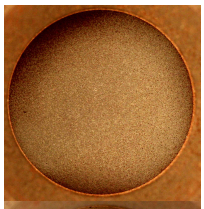
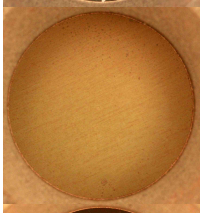
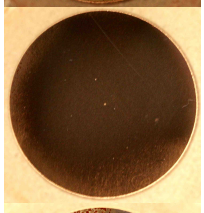
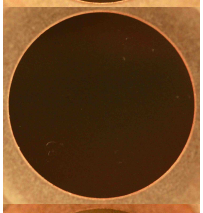
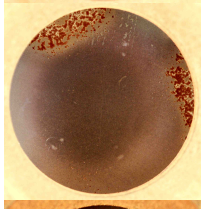
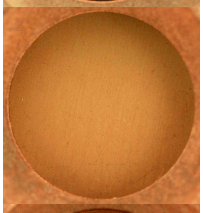
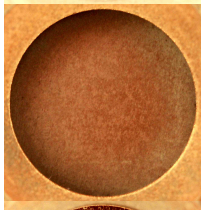
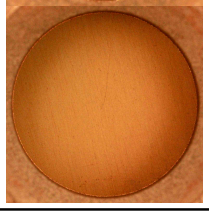
Sample	0 hours	500 hours
3.1 Oxide on no side		
3.2 Oxide on both sides		
3.3 Oxide on anode side		
3.4 Oxide on anode side		
3.5 Oxide on cathode side		
3.6 Oxide on cathode side		

FIGURE 3.10: Photographs taken of run 3. The samples were exposed in dual atmosphere at 600 °C for 500 h. The protective layer was polished off prior to exposure on both sides of sample 3.1, the air facing side of sample 3.3 and 3.4 and the hydrogen facing side of sample 3.5 and 3.6. Prior to the removal all samples were pre-oxidized at 800 °C for 3 h.

3.3.2 Electron Microscopy

The SEM images taken of sample 3.3 are shown in figure 3.11. The result from the visual inspection is confirmed by electron microscopy. Large areas of the sample do not show signs of breakaway corrosion (see figure 3.11 (a)). Furthermore, EDX conducted here confirmed the absence of iron oxide. This is depicted in figure 3.12 and table 3.3. Most of the surface (spectrum 3) is covered by a thin chromium oxide layer. The EDX here shows a comparably high Cr signal. The underlying steel contributes to the signal, too, thus the high amount of iron. Additionally, it can be seen from the EDX results that the bright spots visible in the SEM micrographs are not iron oxide but instead oxides of other alloying elements such as Nb (spectrum 1) or Ti (spectrum 2). In contrast to the nodule-free area in the center of the sample, iron oxide is found on the edge (see figure 3.11 (b)). The onset of breakaway corrosion at the edge is characteristic for all analyzed samples. The reason for that has not yet been thoroughly investigated. A theory is the occurrence of mechanical stresses in the oxide layer due to the fixation of the clamping ring. These stresses are suspected to cause cracks or other defects in the oxide which makes it more prone to corrosion. Another reason for the occurrence of breakaway corrosion primarily at the edge of the sample might be due to chemical interactions with the gold seal. However, further investigations are necessary to explain this behaviour.

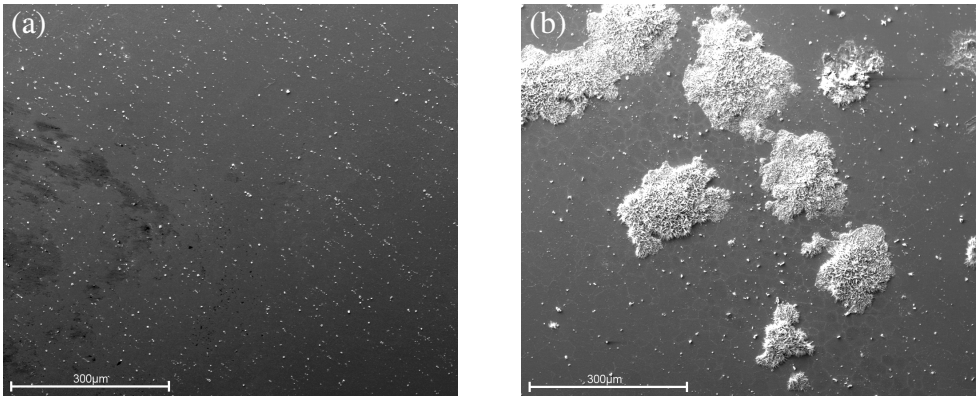


FIGURE 3.11: SEM images taken of the air facing side of sample 3.3 (hydrogen side protection). (a) shows surface which has not undergone breakaway corrosion. In (b) nodules are visible which appear in areas close to the edge of the sample. The sample was exposed in dual atmosphere at 600 °C for 500 h.

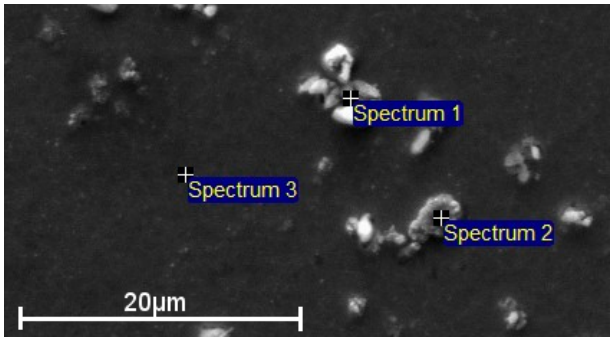


FIGURE 3.12: Spots selected for EDX analysis on a part of the surface of sample 3.3 which had not undergone any breakaway corrosion. The corresponding results are shown in table 3.3. The sample was exposed in dual atmosphere at 600 °C for 500 h.

TABLE 3.3: EDX results of the air facing side of sample 3.3. The corresponding locations of the spectra are shown in figure 3.12. The values are given in atomic% and rounded. The sample was exposed in dual atmosphere at 600 °C for 500 h.

Spectrum	O	Al	Si	Ti	Cr	Mn	Fe	Nb
1	42		0.7	6.2	11	1.0	26	13
2	64	0.2	0.4	23	3.9	2.0	5.5	1.2
3	10		1.1		17	0.7	71	

SEM investigations were also performed on sample 3.5 (protection on air side). The presence of a highly corroded surface was already suspected from visual inspection. This could be confirmed with help of electron microscopy (see figure 3.13). The entire surface is covered with nodules which have grown into a thick uniform layer. No previously existing chromium oxide is visible anymore. EDX was also conducted which confirms the presence of iron oxide (see figure 3.14 and table 3.4). The EDX shows a high content of both iron and oxygen with a low amount of chromium.

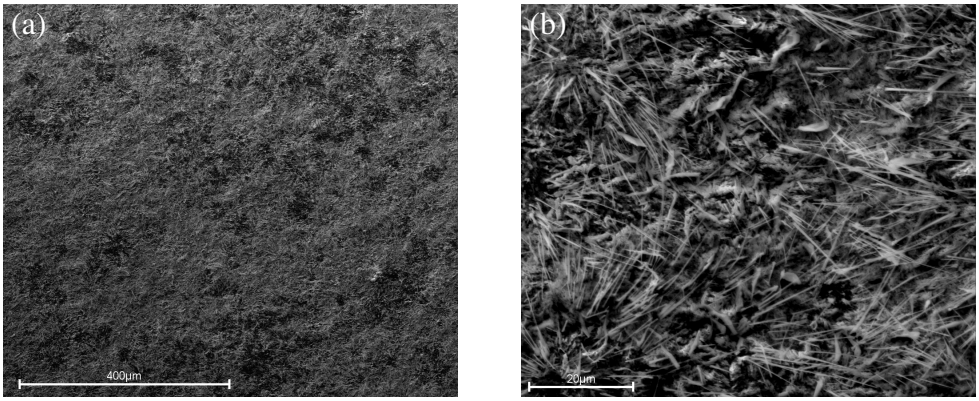
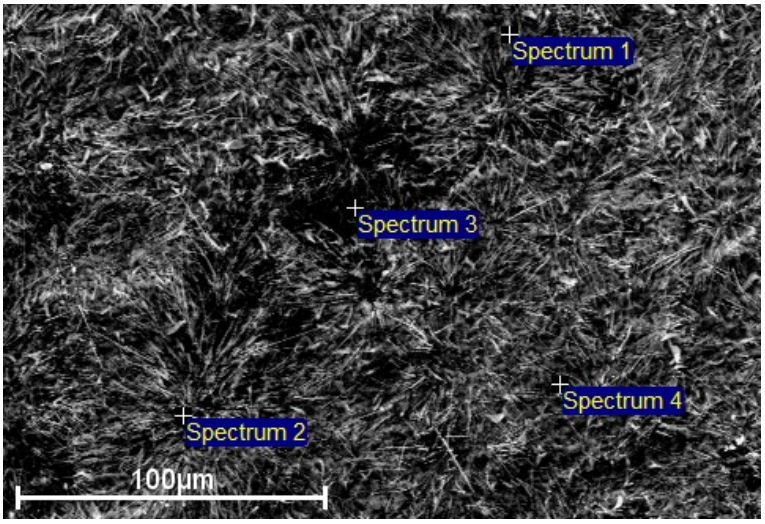


FIGURE 3.13: SEM images taken of the air facing side of sample 3.5. The sample was exposed in dual atmosphere at 600 °C for 500 h.



.

FIGURE 3.14: EDX spectra recorded on the air facing side of sample 3.5. The corresponding results are shown in table 3.4. The sample was exposed in dual atmosphere at 600 °C for 500 h.

TABLE 3.4: EDX spectra as recorded on sample 3.5 with the corresponding locations shown in figure 3.14. The values are given in atomic% and rounded. The sample was exposed in dual atmosphere at 600 °C for 500 h.

Spectrum	O	Cr	Mn	Fe	Cu
1	58	0.2	0.2	42	0.1
2	50	0.2	0.2	49	0.1
3	39	0.2	0.8	60	0.3
4	62	0.2	0.3	37	0.2

Additionally, electron microscopy was conducted on the hydrogen facing side of the samples. The images of sample 3.3, where the hydrogen facing side was not polished prior to exposure are shown in figure 3.15. The surface is covered by a uniform layer with many small bright crystallites. The corresponding EDX results are shown in figure 3.16 and table 3.5. An elevated amount of chromium compared to the alloy composition is found on the surface (spectrum 3). The brighter spots (spectrum 1 and 2) contain an increased amount of titanium and oxygen. These are therefore titanium oxide which is expected to form due to the alloy composition.

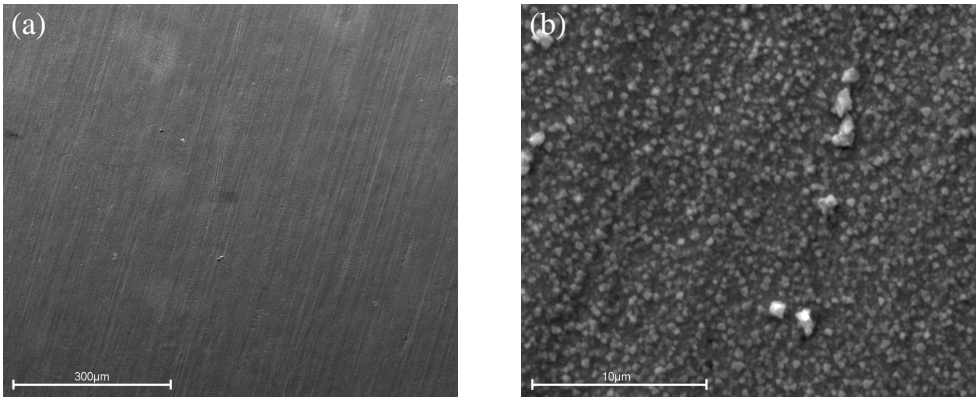


FIGURE 3.15: SEM images taken of the hydrogen facing side of sample 3.3. The sample was exposed in dual atmosphere at 600 °C for 500 h.

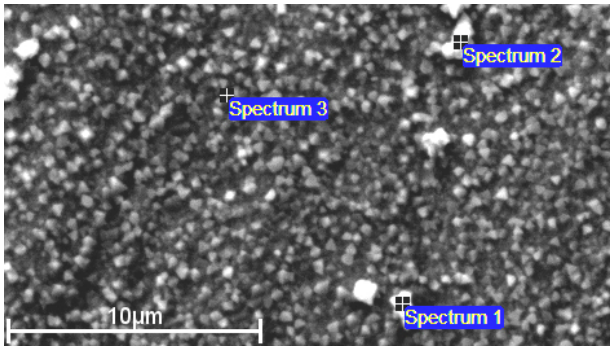


FIGURE 3.16: EDX spectra recorded on the hydrogen facing side of sample 3.3. Results are shown in table 3.5. The sample was exposed in dual atmosphere at 600 °C for 500 h.

TABLE 3.5: EDX spectra as recorded on sample 3.3 corresponding to the spots shown in figure 3.16. The values are given in atomic% and rounded. The sample was exposed in dual atmosphere at 600 °C for 500 h.

Spectrum	O	Si	Ti	Cr	Mn	Fe	Nb
1	61	0.4	10	17	4.7	6	1
2	50	0.6	5.5	27	4.2	11	1.1
3	24	1.1	0.8	20	2.2	52	

The hydrogen facing side of sample 3.5 exhibits a different surface morphology compared to sample 3.3. A large part of the formerly polished surface is covered by crystallites (see figure 3.17). Corresponding EDX measurements are shown in figure 3.18. Elevated amounts of both iron and oxygen and a low amount of chromium are found in spectrum 1 and 2 which were recorded on thick parts of the oxide layer. Due to its morphology and the low oxygen partial pressure on the hydrogen side it is suspected to be magnetite.

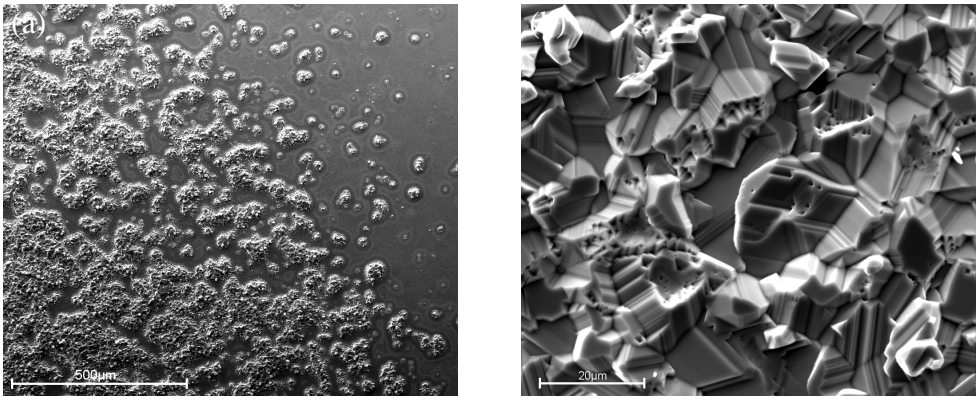


FIGURE 3.17: SEM images taken of the hydrogen facing side of sample 3.5. The sample was exposed in dual atmosphere at 600 °C for 500 h.

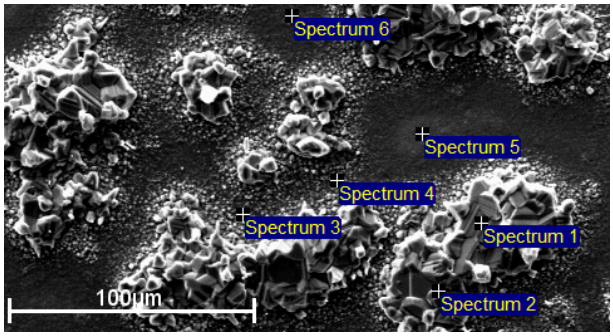


FIGURE 3.18: EDX spectra recorded on the hydrogen facing side of sample 3.5. Results are shown in table 3.6. The sample was exposed in dual atmosphere at 600 °C for 500 h.

TABLE 3.6: EDX spectra as recorded on sample 3.5 according to the spots shown in figure 3.18. The values are given in atomic% and rounded. The sample was exposed in dual atmosphere at 600 °C for 500 h.

Spectrum	O	Si	Ti	Cr	Mn	Fe	Nb
1	52			0.9		47	
2	54			0.8		45	
3	38	1.1		14	0.6	47	
4	59	0.3	2.6	3.5	0.5	33	0.9
5	26	1.1		17	0.9	56	
6	31	1.6		15	0.7	51	

3.3.3 Comparison

A clear difference is detectable between oxide scale on the air side or on the hydrogen side on the samples of run 3. The two which had a protective scale on the air side (samples 3.3 and 3.4), exhibit a thick layer of iron oxide on the air side and even spallation. This was already visible with the naked eye and was further confirmed by electron microscopy. In comparison, the samples which had a protective scale on the hydrogen side show formation of only few iron oxide nodules located mainly at the edge of the sample.
Additionally, iron oxide can be found on the hydrogen facing side of sample 3.3. The hydrogen side of sample 3.5, on the other hand, shows no sign of iron oxide formation. This leads to the conclusion that hydrogen diffusion plays an important role in dual atmosphere corrosion. As hydrogen diffusion through Cr_2O_3 is orders of magnitude slower than diffusion through the alloy, a removal of the protective oxide scale allows for easy hydrogen diffusion through the alloy toward the air facing side. There, it accelerates the chromium evaporation and also blocks the supply of chromium from the alloy to the surface[18,31]. In order to prevent FSS in fuel cells from corroding, the focus should therefore be on avoiding hydrogen diffusion through the alloy. By improving the protection of steel with, for example a protective coating, the diffusion of hydrogen to the air side can be mitigated. This can then inhibit the occurrence of breakaway corrosion and thereby improve the interconnects' lifetime.

4 Conclusion

Ferritic stainless steel (AISI 441) was exposed to dual atmosphere (5% H_2 in 95% Ar on one side and air on the other side) at 600 °C. The samples were pre-oxidized at 800 °C prior to exposure. Subsequently, the protective chromium oxide layers were mechanically removed on either the hydrogen side or the air side. Thereby, the corrosion stability of air side protection versus hydrogen side protection was investigated.

In run 3 it was visible that the protection on the hydrogen side is more important. The air side of the samples which had a protective scale on the hydrogen side did not exhibit severe breakaway corrosion. On the other hand, the samples which had a protective scale on the air side were covered by iron oxide nodules which had grown together to a uniform layer. Additionally, the hydrogen side of these sample also exhibited corrosion, which took place by the formation of magnetite. No iron oxide formation was detected on the samples which had the protective scale on the hydrogen side.

The beneficial effect of pre-oxidation is mainly based on the hydrogen side scale which impedes hydrogen diffusion into the sample. Although the formation of a pre-oxidation scale on the air side is probably also beneficial this protective scale is not sustained when hydrogen can enter the sample unobstructed. This result suggests that the diffusion of hydrogen through the samples plays a major role in dual atmosphere corrosion. However, the exact mechanism behind this has not been thoroughly investigated. In order to prevent steel interconnects from corroding, protective means such as coatings should be applied on the hydrogen side. The focus of these protections should be on mitigating the diffusion speed of hydrogen into the alloy.

5 References

[1] I. Dincer. “Renewable energy and sustainable development: a crucial review”. In: *Renewable and Sustainable Energy Reviews* 4 (2000), pp. 157–175.

[2] I. Dincer. “Environmental impacts of energy”. In: *Energy Policy* 27 (1999), pp. 845–854.

[3] N. Q. Minh. “Ceramic fuel cells”. In: *Journal of the American Ceramic Society* 76 (1993), pp. 563–588.

[4] K. Sukhatme and S. P. Sukhatme. *Solar energy: principles of thermal collection and storage*. 15th ed. Tata McGraw-Hill Education, 2006.

[5] H. Baltruschat. “Differential electrochemical mass spectrometry.” In: *Journal of the American Society for Mass Spectrometry* 15 (2004), pp. 1693–706.

[6] A. Steinfeld. “Solar thermochemical production of hydrogen - A review”. In: *Solar Energy* 78 (2005), pp. 603–615.

[7] S. C. Singhal and K. Kendall. *High temperature solid oxide fuel cells: fundamentals, design and applications*. Elsevier, 2007.

[8] J. Rufner, P. Gannon, P. White, M. Deibert, S. Teintze, R. Smith, and H. Chen. “Oxidation behavior of stainless steel 430 and 441 at 800 C in single (air/air) and dual atmosphere (air/hydrogen) exposures”. In: *International Journal of Hydrogen Energy* 33 (2008), pp. 1392–1398.

[9] J. Wu and X. Liu. “Recent development of SOFC metallic Interconnect”. In: *Journal of Materials Science and Technology* 26 (2010), pp. 293–305.

[10] N. Laosiripojana, W. Wiyaratn, W. Kiatkittipong, A. Arpornwichanop, A. Soottitantawat, and S. Assabumrungrat. “Reviews on solid oxide fuel cell technology”. In: *Engineering Journal* 13 (2009), pp. 65–83.

[11] P. Alnegren. “Environmental effects on degradation of interconnects for solid oxide fuel cells and electrolyzers”. PhD thesis. 2015.

[12] A. B. Stambouli and E. Traversa. “Solid oxide fuel cells (SOFCs): A review of an environmentally clean and efficient source of energy”. In: *Renewable and Sustainable Energy Reviews* 6 (2002), pp. 433–455.

[13] J. D. L. C. Soto and U. C. Castillo. “Fuel Cell as Range Extender in Battery Electric Vehicles for Supply Chain Fleets”. In: *Sustainable Supply Chain Management* (2016), pp. 79–97.

[14] R. P. O’Hayre. *Fuel cell fundamentals*. 3rd ed. John Wiley Sons, 2006, p. 409.

[15] N. Q. Minh and T. Takahashi. *Science and technology of ceramic fuel cells*. 1st ed. Elsevier, 1995.

[16] M. Boaro and A. A. Salvatore. *Advances in medium and high temperature solid oxide fuel cell technology*. Elsevier, 2017.

[17] N. Shaigan, W. Qu, D. G. Ivey, and W. Chen. "A review of recent progress in coatings, surface modifications and alloy developments for solid oxide fuel cell ferritic stainless steel interconnects". In: *Journal of Power Sources* 195 (2010), pp. 1529–1542.

[18] P. Alnegren, M. Sattari, J. E. Svensson, and J. Froitzheim. "Severe dual atmosphere effect at 600°C for stainless steel 441". In: *Journal of Power Sources* 301 (2016), pp. 170–178.

[19] J. Froitzheim, S. Canovic, M. Nikumaa, R. Sachitanand, L. G. Johansson, and J. E. Svensson. "Long term study of Cr evaporation and high temperature corrosion behaviour of Co coated ferritic steel for solid oxide fuel cell interconnects". In: *Journal of Power Sources* 220 (2012), pp. 217–227.

[20] P. Kofstad. *High temperature corrosion*. 1st ed. Springer, 1988.

[21] Z. Yang, K. S. Weil, D. M. Paxton, and J. W. Stevenson. "Selection and evaluation of heat-resistant alloys for SOFC interconnect applications". In: *Journal of The Electrochemical Society* 150 (2003), A1188.

[22] D. A. Jones. *Principles and prevention of corrosion*. 2nd ed. Pearson, 1996, p. 412.

[23] P. Alnegren. "Oxidation behavior of selected FeCr alloys in environments relevant for solid oxide electrolysis applications". PhD thesis. 2012.

[24] H. Kurokawa, K. Kawamura, and T. Maruyama. "Oxidation behavior of Fe-16Cr alloy interconnect for SOFC under hydrogen potential gradient". In: *Solid State Ionics* 168 (2004), pp. 13–21.

[25] H. Kaesche. *Corrosion of metals: physicochemical principles and current problems*. Springer Science Business Media, 2003, pp. 193–202.

[26] X. Chen, P. Y. Hou, C. P. Jacobson, S. J. Visco, and L. C. De Jonghe. "Protective coating on stainless steel interconnect for SOFCs: Oxidation kinetics and electrical properties". In: *Solid State Ionics* 176 (2005), pp. 425–433.

[27] E. W. A. Young. "The oxygen partial pressure dependence of the defect structure of Chromium(III)Oxide". In: *Journal of The Electrochemical Society* 134 (1987), p. 2257.

[28] M. J. Graham and R. J. Hussey. “Analytical techniques in high temperature corrosion”. In: *Oxidation of Metals* 44 (1995), pp. 339–374.

[29] J. G. Grolig, J. Froitzheim, and J. E. Svensson. “Coated stainless steel 441 as interconnect material for solid oxide fuel cells: oxidation performance and chromium evaporation”. In: *Journal of Power Sources* 248 (2014), pp. 1007–1013.

[30] H. Falk-Windisch, J. E. Svensson, and J. Froitzheim. “The effect of temperature on chromium vaporization and oxide scale growth on interconnect steels for solid oxide fuel cells”. In: *Journal of Power Sources* 287 (2015), pp. 25–35.

[31] Z. Yang, M. S. Walker, P. Singh, J. W. Stevenson, and T. Norby. “Oxidation behavior of ferritic stainless steels under SOFC interconnect exposure conditions”. In: *Journal of The Electrochemical Society* 151 (2004), B669.

[32] C. Ostwald and H. J. Grabke. “Initial oxidation and chromium diffusion. I. Effects of surface working on 9-20% Cr steels”. In: *Corrosion Science* 46 (2004), pp. 1113–1127.

[33] L. Niewolak, E. Wessel, L. Singheiser, and W. J. Quadakkers. “Potential suitability of ferritic and austenitic steels as interconnect materials for solid oxide fuel cells operating at 600°C”. In: *Journal of Power Sources* 195 (2010), pp. 7600–7608.

[34] P. Alnegren. *unpublished results*. 2017.

[35] C. Goebel. *unpublished results*. 2017.

[36] P. Goodhew and F. Humphreys. *Electron microscopy and analysis*. 2nd ed. CRC Press, 1988.

[37] W. Zhang, J. Li, J. Yang, B. Zhou, B. Chi, J. Pu, and L. Jian. “Characterization of a new Fe-based alloy as metallic interconnect in SOFC anode environment”. In: *International Journal of Hydrogen Energy* 41 (2016), pp. 22246–22253.